# Attractive and repulsive dipolar interaction in bilayers of indirect excitons

D. J. Choksy [1] Chao Xu,[1] M. M. Fogler,[1] L. V. Butov,[1] J. Norman,[2] and A. C. Gossard[2]

[1]*Department of Physics, University of California at San Diego, La Jolla, California 92093-0319, USA*
[2]*Materials Department, University of California at Santa Barbara, Santa Barbara, California 93106-5050, USA*

We explore attractive dipolar interaction in indirect excitons (IXs). For one layer of IXs in a single pair of coupled quantum wells (CQWs), the out-of-plane IX electric dipoles lead to repulsive dipolar interaction between IXs. The attractive dipolar interaction between IXs is realized in a two-CQW heterostructure with two IX layers in two separated CQW pairs. We found both in experimental measurements and theoretical simulations that increasing density of IXs in one layer causes a monotonic energy reduction for IXs in the other layer. We also found an in-plane shift of a cloud of IXs in one layer towards a cloud of IXs in the other layer. This behavior is qualitatively consistent with attractive dipolar interaction. The measured IX energy reduction and IX cloud shift are higher than the values given by the correlated liquid theory.

## I. INTRODUCTION

A spatially indirect exciton (IX), also known as an interlayer exciton, is a bound pair of an electron and a hole confined in separated layers. Due to the electron-hole separation, IXs have built-in electric dipole moment $ed$, where $d$ is the distance between the electron and the hole layers, and $e$ is the electron charge. Furthermore, due to the electron-hole separation, IXs have long lifetimes within which they can cool below the temperature of quantum degeneracy [1]. These properties make IXs a platform for exploring quantum gases with dipolar interaction.

IXs can be realized in a pair of quantum wells separated by a narrow tunneling barrier. For one layer of IXs in a single pair of coupled quantum wells (CQWs), the out-of-plane IX electric dipoles lead to repulsive dipolar interaction between side-to-side IX dipoles (Fig. 1). This configuration is extensively studied both theoretically and experimentally. The phenomena originating from the repulsive dipolar interaction in a single IX layer include the enhancement of IX energy with density that has been known since early studies of IXs [2–6], screening of the in-plane disorder potential by repulsively interacting IXs [7–10] that leads to IX delocalization and long-range IX transport [7–18], strong correlations [10,19–26], and predicted crystal phases [27–32].

Quantum gases with dipolar interaction are also explored with cold atoms. In these systems, dipolar interactions lead to droplet structures with spatial ordering and coherence [36–40], few-body complexes [41,42], and a pair of superfluid and crystal phases in bilayers of dipoles [43–46].

The specific property of dipolar interaction is its anisotropy. For instance, for two parallel dipoles tilted at angle $\theta$ relative to the line connecting them, the interaction at $r \gg d_1, d_2$ is given by $v(r) \sim e^2 d_1 d_2 (1-3\cos^2\theta)/\epsilon r^3$, where $\epsilon$ is the dielectric constant of the material and $p_{1,2} = ed_{1,2}$ are the dipole moments [47]. For the out-of-plane IX dipoles in a single IX layer this expression reduces to $v(r) \sim e^2 d^2/\epsilon r^3$ describing the repulsive dipolar interaction between IXs.

The other specific property of dipolar interaction for the IXs is the induced orientation of IX dipoles. The heterostructure design and/or applied voltage, which produces the electric field in the heterostructure, determine the quantum well layers where electrons and holes are confined: Exchanging the quantum wells by the electron and the hole, i.e., flipping the IX dipole, is energetically unfavorable. Furthermore, tilting the IX dipole relative to the $z$ direction causes an in-plane separation of the electron and the hole in the IX and, as a result, reduces the IX binding energy. This induces the orientation of IX dipoles in the direction normal to the QW plane.

The induced orientation of the IX dipoles and the repulsive dipolar interaction for a single IX layer makes it challenging to explore the attractive dipolar interaction in IX systems. The studies of IX dipoles have been concentrated on the case of repulsively interacting IXs [1–31]. However, the angle-dependent dipolar IX interaction and, in particular, dipolar attraction give access to new phenomena in quantum dipolar gases. For instance, the dipolar attraction leads to the phenomena in cold atoms outlined above [36–46]. IX attraction can be realized by extending IX heterostructures beyond a single CQW design, and studies of attractively interacting IX dipoles were recently started in two stacked CQW pairs [48–50].

In this paper, we explore the attractive dipolar interaction between IXs in a two-CQW heterostructure with two IX layers in two separated CQW pairs (Fig. 1). The intra-CQW interaction between IX side-to-side dipoles is repulsive similar to single CQW heterostructures [1–31]. The inter-CQW interaction between IX head-to-tail dipoles is attractive. It changes to repulsive with increasing in-plane separation between the IXs and, in turn, $\theta$ following the anisotropy of dipolar interaction outlined above. Both our experimental measurements and our theoretical simulations show: (i) a monotonic energy reduction for IXs in one layer with increasing density of IXs in the other layer, and (ii) an in-plane shift of a cloud of IXs in one layer towards a cloud of IXs in the other layer. This behavior is qualitatively consistent with attractive dipolar interaction,
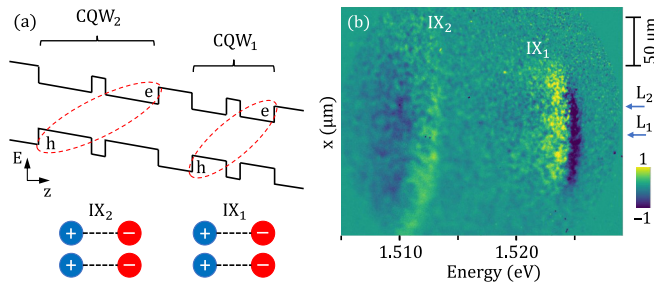
FIG. 1. Two-CQW heterostructure and *x*-energy image. (a) Diagram of the two-CQW structure with two CQW pairs. $IX_2$ forms in $CQW_2$, and $IX_1$ forms in $CQW_1$. Schematic below shows IX dipoles. $-$ electrons and $+$ holes. The intra-CQW interaction between $IX_2$ (or $IX_1$) side-to-side dipoles is repulsive. The inter-CQW interaction between $IX_2$ and $IX_1$ head-to-tail dipoles is attractive. (b) Differential *x*-energy luminescence image. The arrows indicate the excitation spot positions of the $L_2$ and $L_1$ lasers resonant to direct excitons in 15-nm $CQW_2$ and 12-nm $CQW_1$, respectively. $L_2$ generates $IX_2$. $L_1$ generates $IX_1$ and a smaller concentration of $IX_2$. The laser powers $P_{L1} = 10 \ \mu W$, $P_{L2} = 250 \ \mu W$. The differential *x*-energy image is obtained by subtracting the *x*-energy images created by only $L_1$ on and by only $L_2$ on from the *x*-energy image created by both lasers on. In the differential *x*-energy image, the yellow and blue colors indicate the enhancement and reduction of the IX luminescence intensity, respectively. For the energy axis, the blue region on the right side and the yellow region on the left (observed for $IX_1$) correspond to an energy decrease. For the position axis, the blue region on the low side and the yellow region on the high side (observed for $IX_1$) correspond to a cloud shift up. The differential *x*-energy image shows an increase in $IX_2$ energy, a decrease in $IX_1$ energy, and a spatial shift of the $IX_1$ cloud towards the $IX_2$ cloud.

however, the measured IX energy reduction and IX cloud shift are higher than the values given by the correlated liquid theory.

## II. EXPERIMENT

The studied two-CQW heterostructure [Fig. 1(a)] is grown by molecular beam epitaxy. Indirect excitons $IX_2$ form in $CQW_2$, indirect excitons $IX_1$ form in $CQW_1$. $CQW_2$ consists of two 15-nm GaAs QWs separated by a 4-nm $Al_{0.33}Ga_{0.67}As$ barrier, $CQW_1$ consists of two 12-nm GaAs QWs separated by a 4-nm $Al_{0.33}Ga_{0.67}As$ barrier. $CQW_2$ and $CQW_1$ are separated by a 12-nm $Al_{0.33}Ga_{0.67}As$ barrier, narrow enough to allow substantial interlayer interaction between $IX_2$ and $IX_1$, yet wide enough to suppress tunneling of electrons and holes between $CQW_2$ and $CQW_1$. $n^+$-GaAs layer with $n_{Si} \sim 10^{18} \ cm^{-3}$ serves as a bottom electrode. The CQW pair is positioned 100 nm above the $n^+$-GaAs layer within the undoped 1-$\mu$m-thick $Al_{0.33}Ga_{0.67}As$ layer. The two CQW pairs are positioned closer to the homogeneous bottom electrode to suppress the fringing in-plane electric field in excitonic devices [51]. The top semitransparent electrode is fabricated by applying 2-nm Ti and 7-nm Pt on a 7.5-nm GaAs cap layer. Applied gate voltage $V_g = -2$ V creates an electric field in the *z* direction. The cross section of the heterostructure is presented in Appendix D.

The $IX_2$ energy is lower than the $IX_1$ energy. This energy difference gives an opportunity to selectively generate $IX_2$ by optical excitation. Excitons are generated by semiconductor lasers $L_2$ and $L_1$ at the energies 1.532 and 1.541 eV resonant to spatially direct excitons (DXs) in $CQW_2$ and $CQW_1$, respectively. The resonant to DX excitation increases the light absorption and, in turn, IX density for a given laser power [52]. $L_2$ generates $IX_2$. $L_1$ generates $IX_1$ and roughly a two times smaller concentration of $IX_2$ due to a weaker nonresonant absorption of $L_1$ light in $CQW_2$. $L_2$ and $L_1$ excitations are focused to $\sim 5$-$\mu$m half width at half maximum spots, which are separated by 50 $\mu$m. This configuration allows exploring the effects of IX interactions on the IX cloud position. IX photoluminescence (PL) is measured in a 20-ns time window starting 20 ns after the end of the $L_1$ and/or $L_2$ excitation pulses. This allows for studying of only long-lived IXs after DXs recombined. Both $IX_2$ and $IX_1$ have long lifetimes in the range of hundreds of nanoseconds ($\sim 800$ ns for $IX_2$ and $\sim 260$ ns for $IX_1$) allowing them to travel over long distances reaching hundreds of microns.

Time-resolved imaging experiments are performed with a laser pulse duration 2000 ns, period 4000 ns, and edge sharpness $\sim 2$ ns. The rectangular-shaped pulses are realized by a pulse generator driving the semiconductor lasers. The pulse duration and period are optimized to allow the IX PL image to approach equilibrium during the laser excitation and decay between laser pulses. The PL images are captured using a PicoStar HR TauTec time-gated intensifier. The PL passes through a spectrometer with a resolution of 0.18 meV before entering the intensifier coupled to a liquid-nitrogen-cooled CCD. The measurements are performed at $T_{bath} = 1.7$ K.

To analyze the attractive interlayer IX interaction in the IX bilayer we measure how the selective generation of $IX_2$ affects the energies and cloud position of $IX_1$. Figure 1(b) presents the differential *x*-energy image obtained by subtracting the *x*-energy images created by only $L_1$ on [Fig. 10(c) in Appendix C] and by only $L_2$ on [Fig. 10(b)] from the *x*-energy image created by both lasers on simultaneously [Fig. 10(a)]. The differential *x*-energy image shows an increase in $IX_2$ energy, a decrease in $IX_1$ energy, and a spatial shift of the $IX_1$ cloud towards the $IX_2$ cloud. These phenomena are detailed below.

First, we consider the IX energy variations. Figures 2(a)–2(c) show that the increase in $L_2$ power ($P_{L2}$) and, in turn, $IX_2$ density ($n_2$) leads to a monotonic decrease in $IX_1$ energy. An energy decrease corresponds to attractive $IX_1$-$IX_2$ interaction. In comparison, when only $IX_2$'s are present in the system ($L_1$ is off), the increase in $P_{L2}$ and, in turn, $n_2$ leads to a monotonic increase in $IX_2$ energy [Figs. 2(d)–2(f)]. An energy increase corresponds to repulsive $IX_2$-$IX_2$ interaction, which has been extensively studied in single layers of IXs [1–31].

Figures 2(c) and 2(f) also show that the increase in $P_{L1}$ leads to a monotonic increase in both $IX_1$ and $IX_2$ energies. $L_1$ generates both $IX_1$ and $IX_2$, therefore, the effect of increasing $P_{L1}$ on $IX_1$ (or $IX_2$) energy is a combined effect of attractive $IX_1$-$IX_2$ and repulsive $IX_1$-$IX_1$ (or $IX_2$-$IX_2$) interactions. The monotonic increase in both $IX_1$ and $IX_2$ energies with $P_{L1}$ indicates that the repulsive interaction is stronger. This is consistent with the relative strength of the attractive [Fig. 2(a)]
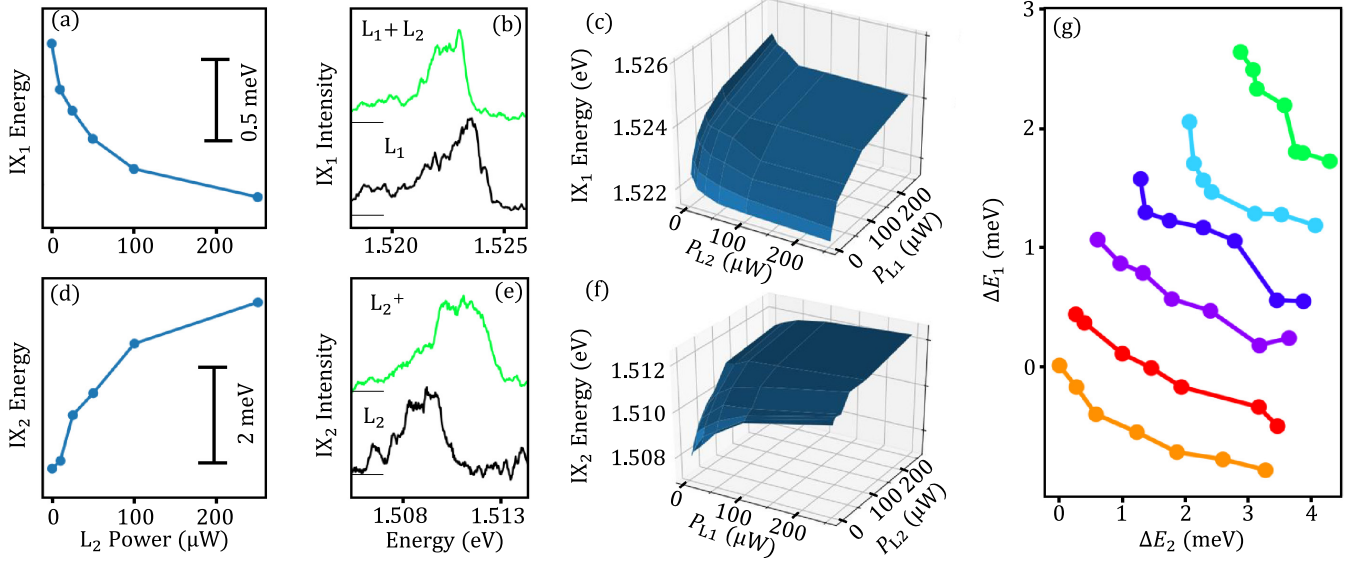
FIG. 2. Decrease and increase of IX energy due to attractive and repulsive dipolar IX interactions: Experiment. (a) The decrease in $IX_1$ energy with increasing $L_2$ power and, in turn, $IX_2$ density. $P_{L1} = 10 \,\mu W$. An energy decrease corresponds to attractive $IX_1$-$IX_2$ interaction. (b) The redshift of the $IX_1$ spectrum with turning on $L_2$, which increases $IX_2$ density. The black line shows the $IX_1$ spectrum when only $L_1$ is on, $P_{L1} = 10 \,\mu W$. The green line shows the $IX_1$ spectrum when an additional $L_2$ is on, $P_{L2} = 250 \,\mu W$. (c) $IX_1$ energy as a function of both $P_{L1}$ and $P_{L2}$. (d) The increase in $IX_2$ energy with increasing $L_2$ power and, in turn, $IX_2$ density. $P_{L1} = 0$. An energy increase corresponds to repulsive $IX_1$-$IX_2$ interaction. (e) The blueshift of the $IX_2$ spectrum with increasing $L_2$ power, which increases $IX_2$ density. $P_{L2} = 25 \,\mu W$ (black line) and $250 \,\mu W$ (green line). (f) $IX_2$ energy as a function of both $P_{L1}$ and $P_{L2}$. (g) The change in $IX_1$ energy vs the change in $IX_2$ energy. Each set of data corresponds to increasing $L_2$ power. For the sets of data presented by orange, red, purple, blue, cyan, and green points, $L_1 = 5, 10, 25, 50, 100$, and $250 \,\mu W$, respectively.

and repulsive [Fig. 2(d)] interaction in the experiments with increasing $P_{L2}$ which increase only $IX_2$ density.

In the mean-field approximation the repulsive interaction between IXs in a single layer increases the IX energy by $\Delta E = 4\pi e^2 dn/\epsilon$. This equation known as the "plate capacitor" formula provides a qualitative explanation for the observed monotonic increase in $\Delta E$ with the exciton density $n$ [2]. However, the capacitor formula can significantly overestimate $\Delta E(n)$ due to the IX correlations [10,19–26]. To compare the attractive and repulsive dipolar interactions, avoiding the complexity of the relation between $\Delta E$ and $n$, Fig. 2(g) presents the change in $IX_1$ energy $\Delta E_1$ vs the change in $IX_2$ energy $\Delta E_2$ for the data in Figs. 2(c) and 2(f). The energy shifts $\Delta E$ are measured relative to the IX energies at the lowest $n$. Figure 2(g) shows that for all studied $P_{L1}$'s, the increase in $P_{L2}$ and, in turn, $n_2$ leads to $\Delta E_2$ larger in absolute value than $\Delta E_1$, indicating that the repulsive $IX_2$-$IX_2$ interaction is stronger than the attractive $IX_2$-$IX_1$ interaction.

We also consider the spatial shift of the $IX_1$ cloud toward the $IX_2$ cloud [53]. Figure 3 shows that the $IX_1$ cloud attracts to the $IX_2$ cloud. With increasing $P_{L2}$, the spatial shift is nonmonotonic. This behavior is observed for different $P_{L1}$'s. A larger spatial shift, reaching $\sim 10 \,\mu m$, is observed at low $P_{L1}$ [Fig. 3(b)].

### III. THEORY

We analyze the dipolar interaction in IX bilayers theoretically and compare the experimental data with theoretical simulations. The numerical simulation of a such two-species many-body system is performed through the hypernetted

chain (HNC) formalism [54]. The intra- and interlayer interactions are modeled by assuming that the wave function of electrons and holes are isotropic Gaussians and they experience a Coulomb interaction, see Appendix A. The HNC method has been previously used for studying bosons with dipolar interactions in single-layer systems [55]. Unless the interaction strength is very high, the HNC predictions for basic many-body properties, such as pair-correlation functions and energy per particle were shown to be in good agreement with the more accurate Monte Carlo calculations [29,45,46].
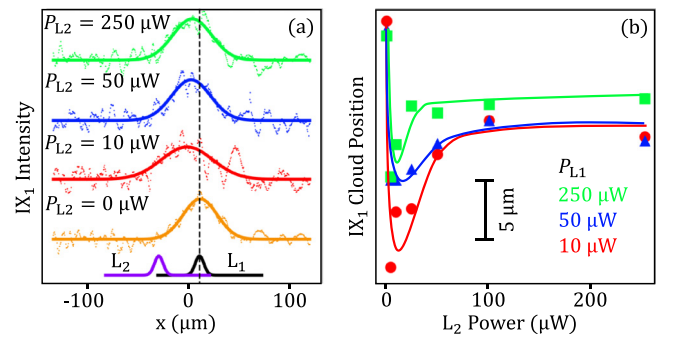


FIG. 3. Attraction of the $IX_1$ cloud to the $IX_2$ cloud: Experiment. (a) The $IX_1$ cloud profiles at different $P_{L2}$'s and, in turn, $IX_2$ densities. $P_{L1} = 10 \,\mu W$. The profiles of the $L_1$ and $L_2$ laser excitation spots are shown by black and purple lines, respectively. The dashed line indicates the center of the $L_1$ excitation spot. (b) The center-of-mass position of the $IX_1$ cloud as a function of $P_{L2}$ for different $P_{L1}$'s.
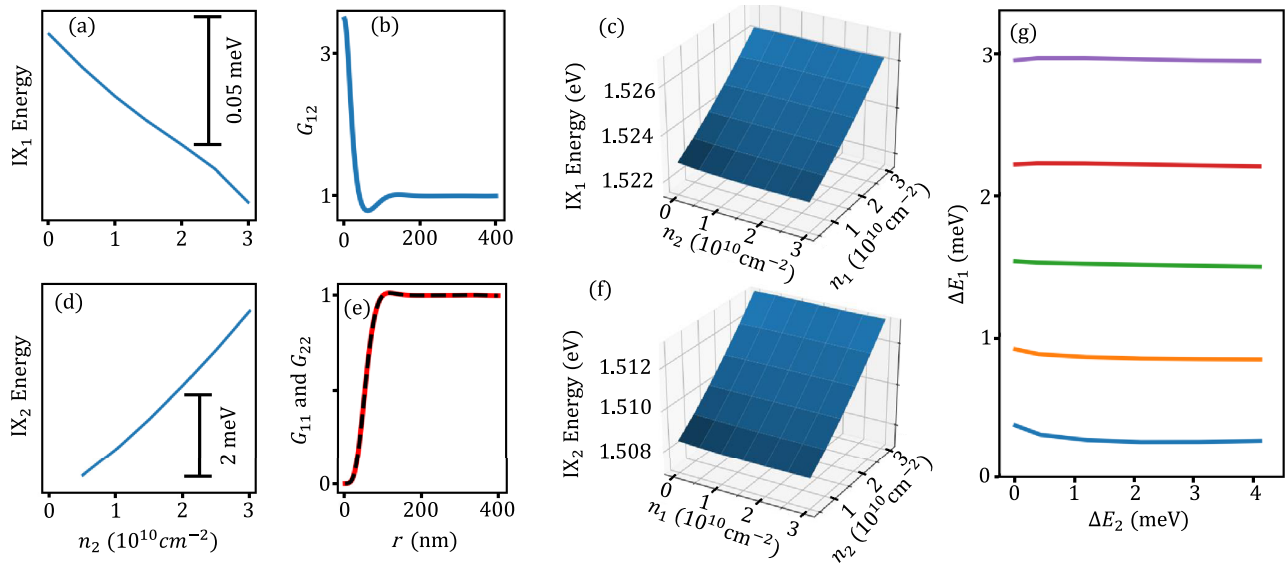
FIG. 4. Decrease and increase in IX energy due to attractive and repulsive dipolar IX interactions: Theory. (a) The decrease in $IX_1$ energy with increasing $IX_2$ density. $n_1 = 1.5 \times 10^{10}$ cm$^{-2}$. An energy decrease corresponds to attractive $IX_2$-$IX_1$ interaction. (b) $IX_1$-$IX_2$ density correlation function. $n_1 = n_2 = 10^{10}$ cm$^{-2}$. (c) $IX_1$ energy as a function of both $IX_1$ and $IX_2$ densities. (d) The increase in $IX_2$ energy with increasing $IX_2$ density. $n_1 = 0$. An energy increase corresponds to repulsive $IX_2$-$IX_2$ interaction. (e) $IX_2$-$IX_2$ (red solid line) and $IX_1$-$IX_1$ (black dashed line) density correlation functions. $n_1 = n_2 = 10^{10}$ cm$^{-2}$. (f) $IX_2$ energy as a function of both $IX_1$ and $IX_2$ densities. (g) The change in $IX_1$ energy vs the change in $IX_2$ energy. Each line corresponds to increasing $IX_2$ density. For the blue, orange, green, red, and purple lines, $n_1 = 0.5,\ 1,\ 1.5,\ 2,$ and $2.5 \times 10^{10}$ cm$^{-2}$, respectively.

The simulated IX energy shifts caused by the attractive and repulsive IX dipolar interactions are presented in Fig. 4. Figures 4(a) and 4(c) show that the increase in $n_2$ leads to a monotonic decrease in $IX_1$ energy due to the attractive $IX_1$-$IX_2$ interaction, in qualitative agreement with the experimental data in Figs. 2(a) and 2(c). In contrast, the increase in $n_2$ (or $n_1$) leads to a monotonic increase in $IX_2$ (or $IX_1$) energy [Figs. 4(d) and 4(f)] due to the repulsive $IX_2$-$IX_2$ (or $IX_1$-$IX_1$) interaction, in qualitative agreement with the experimental data in Figs. 2(d) and 2(f).

In the simulations, $n_1$ is increased selectively keeping $n_2$ intact. In the experiment, an increase in $n_1$ is accompanied by an increase in $n_2$ as outlined above. This leads to different variations of $IX_2$ energy with $n_1$ in the experiment [Fig. 2(f)] and the theory [Fig. 4(f)]. However, the conclusions on the attractive $IX_1$-$IX_2$ interaction and repulsive $IX_2$-$IX_2$ interaction derived from the experiment and the comparison between the experiment and the theory are based on the $n_2$ dependence and are not affected by the difference in the $n_1$ dependence.

The density correlation functions for the cases of attractive $IX_1$-$IX_2$ and repulsive $IX_1$-$IX_1$ and $IX_2$-$IX_2$ interactions are presented in Figs. 4(b) and 4(e), respectively. For the attractively interacting IXs [Fig. 4(b)], the correlation function enhancement above 1, the mean-field value, increases the interaction energy compared with the vanishing interlayer interaction in the mean-field approximation. On the contrary, the repulsively interacting IXs avoid each other [Fig. 4(e)] that lowers the intralayer IX interaction energy compared with the uncorrelated state assumed in the mean-field approximation.

The energy shift in Fig. 4(d) is close to 1/3 of the shift given by the plate capacitor formula, in other words, the exciton density is related to the measured energy shift caused by the intralayer IX interaction by the formula $\Delta E \sim 1/3 \times 4\pi e^2 dn/\epsilon$. In Figs. 2(d) and 4(d), the ranges of the energy shift in the experiment and the theory are similar so that the range of the $L_2$ laser power in Fig. 2(d) approximately corresponds to the range of the exciton density $n_2$ in Fig. 4(d).

As for the experimental data, we compare the attractive and repulsive dipolar interactions in a graph showing $\Delta E_1$ vs $\Delta E_2$. Figure 4(g) shows that for all studied $n_1$, the increase in $n_2$ leads to calculated $\Delta E_2$ larger in absolute value than $\Delta E_1$, in qualitative agreement with the experimental data in Fig. 2(g).

We also simulated the spatial shifts of the $IX_1$ cloud toward the $IX_2$ cloud. The simulations of the IX spatial profiles are based on the IX generation, diffusion, and recombination and are outlined in Appendix B. Figure 5 shows that the $IX_1$ cloud attracts to the $IX_2$ cloud in the simulations, in qualitative agreement with the attraction observed in the experiment (Fig. 3). In comparison, both our experimental measurements (Fig. 8) and theoretical simulations (Fig. 9) show that two clouds of repulsively interacting $IX_2$ repel each other, see Appendix B.

Although both the experimental measurements and the theoretical simulation show: (i) a monotonic $IX_1$ energy reduction with increasing $IX_2$ density, and (ii) an in-plane shift of $IX_1$ cloud towards the $IX_2$ cloud, consistent with attractive dipolar interaction, the measured $IX_1$ energy reduction and $IX_1$ cloud shift are higher than the values given by the correlated liquid theory [compare Fig. 2(a) with Fig. 4(a), Fig. 2(g) with Fig. 4(g), and Fig. 3 with Fig. 5]. The interaction- and/or disorder-induced IX mass enhancement may be one possible reason for this discrepancy. The magnitude of $IX_1$ energy reduction $\Delta E_1$ scales with the strength of interlayer $IX_1$-$IX_2$ dipolar attraction (Fig. 6). For the case of a single $IX_1$-$IX_2$
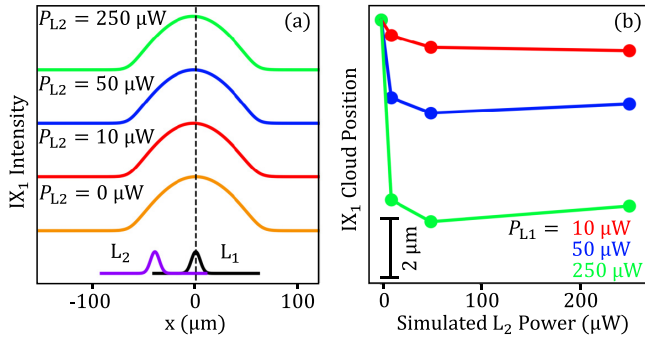
FIG. 5. Attraction of the $IX_1$ cloud to the $IX_2$ cloud: Theory. (a) The $IX_1$ cloud profiles simulated for different $P_{L2}$'s and, in turn, $IX_2$ densities. $P_{L1} = 250\ \mu W$. The profiles of the $L_1$ and $L_2$ laser excitation spots are shown by black and purple lines, respectively. The dashed line indicates the center of the $L_1$ excitation spot. (b) The center-of-mass position of the $IX_1$ cloud as a function of $P_{L2}$ for different $P_{L1}$'s.

pair, $\Delta E_1$ can be estimated as the binding energy of $IX_1$-$IX_2$ biexciton state $E_b$. For a bare IX mass $m_{IX} \sim 0.2 m_0$ [56], $E_b \sim 0.3$ meV (Fig. 7). Higher $E_b$ can be achieved for higher IX masses, and, e.g., for the reduced IX mass enhanced to $2m_0$, $E_b$ reaches $\sim 1.2$ meV (Fig. 7), making the $IX_1$-$IX_2$ interaction scale comparable to the experiment (Fig. 2). A mass enhancement can be caused by interaction, however, only a relatively weak interaction-induced mass enhancement, up to $\sim 25\%$, was observed in electron-hole systems in single QWs [57]. The studies of effects of interaction and/or disorder on the IX mass can be a subject of future work.

Layered heterostructures with more than one IX layer, such as IX bilayers in this paper, and, generally, with more than two
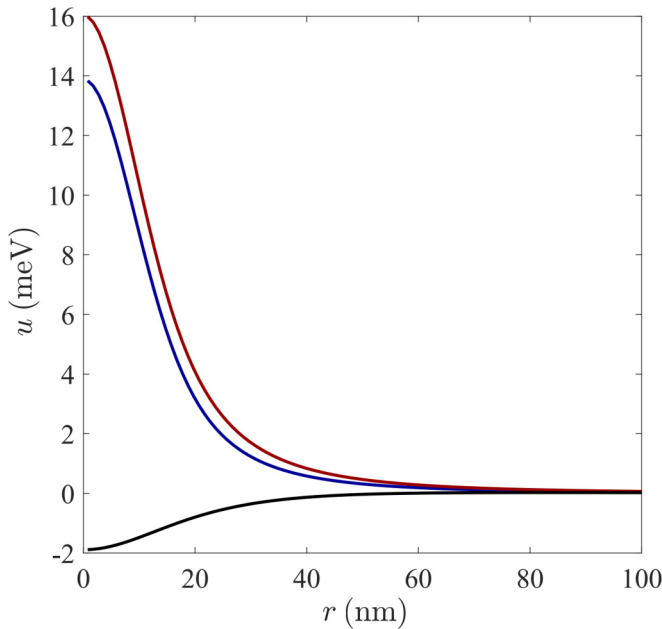


FIG. 6. Model interaction potentials: $u_{22}$ (top) and $u_{11}$ (middle) are the intra-$CQW$ potentials for $IX_2$ and $IX_1$, respectively; $u_{12}$ (bottom curve) is the inter-$CQW$ interaction potential. Parameters: $d_1 = 20$, $d_2 = 25$, $D = 43$, $a = 5$ (all in nanometers); $\epsilon = 13$.
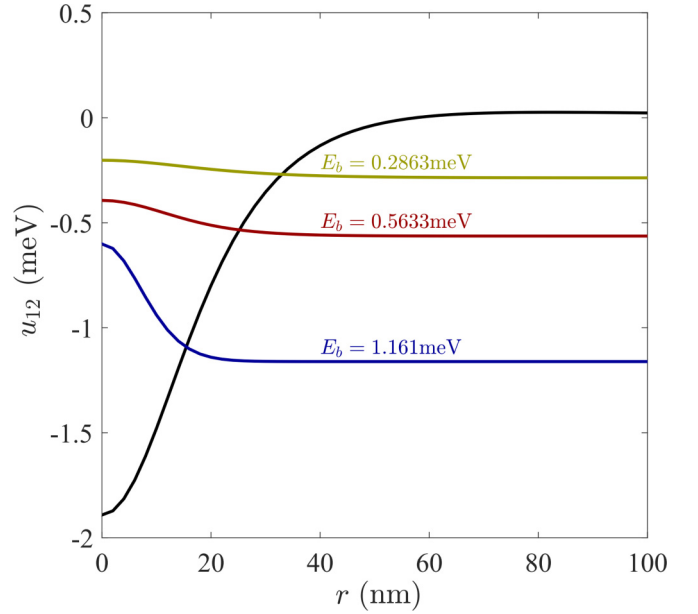


FIG. 7. Probability density distributions of inter-$CQW$ biexcitons within the rigid-body approximation. The interaction potential $u_{12}$ (the same as in Fig. 6) is shown by the curve with a dip (black curve). The probability distributions (wave functions squared) of the bound states are depicted by the curves with the maxima. These curves are plotted in arbitrary units and are offset to show the binding energies $E_b$. They correspond (top to bottom) to the reduced masses of 0.5, 1, and 10 of the exciton mass.

electron and hole layers, such as three-layer heterostructures in Ref. [58], could be new platforms for studying systems with attractive dipolar interaction. For heterostructures with a fixed set of materials, the range of parameter variation may be limited. For instance, for the GaAs/AlGaAs heterostructures used in this paper, it is difficult to achieve a significant change in the dipolar attraction between the IXs by varying the AlGaAs spacer layer thickness $d_s$: A significant reduction of $d_s$ would lead to substantial tunneling of electrons and holes between $CQW_1$ and $CQW_2$, destroying both $IX_1$ and $IX_2$, whereas a significant enhancement of $d_s$ would lead to a substantial reduction of the dipolar interaction, which drops as $1/r^3$ and is already weak for $d_s = 12$ nm in the heterostructure studied in this paper.

However, a significant change in the parameters can be achieved by using different materials. In particular, van der Waals heterostructures offer an opportunity to study IX bilayers with small $d$ and/or $d_s$ (significantly smaller than in the GaAs heterostructures) and high IX binding energies (significantly higher than in the GaAs heterostructures), see Ref. [59] and references therein. The studies of dipolar interactions in IX bilayers and other IX systems with multiple electron and hole layers in van der Waals heterostructures can be a subject of future work.

## IV. CONCLUSION

To summarize, we presented experimental and theoretical studies of attractive dipolar interaction in IX bilayers. We found that increasing density of IXs in one layer causes a

monotonic energy reduction for IXs in the other layer. We also found an in-plane shift of a cloud of IXs in one layer towards a cloud of IXs in the other layer. This behavior is qualitatively consistent with attractive dipolar interaction. The measured IX energy reduction and IX cloud shift are higher than the values given by the correlated liquid theory.

## APPENDIX A: EXCITON INTERACTION

### 1. Interaction potentials

We modeled IXs as composite bosonic particles with a rigid internal charge distribution. The interactions of such particles can be specified in terms of potentials $u_{ij}(r)$, $1 \leqslant i$, $j \leqslant 2$, which are functions of pairwise in-plane distances $r$ of the excitons. We use subscripts 1 and 2 to label the CQWs (12-nm and 15-nm wide, respectively). To compute these interaction potentials, we assumed that the charge distributions of all the electrons and holes are spherically symmetric Gaussians. The radius $a$ of the Gaussians is our adjustable parameter that accounts for the width of the quantum wells and the internal motion of particles about the center of mass of each exciton. We computed these interaction potentials by taking the convolutions of the Coulomb kernel $e^2/\epsilon\sqrt{r^2 + z^2}$ with the charge densities of the interacting particle pairs. The result for the inter-CQW potential $u_{12}(r) = u_{21}(r)$ is

$$u_{12}(r) = \sum_{\sigma=\pm}\sum_{\tau=\pm} V\left(\sqrt{r^2 + z_{\sigma\tau}^2}\right), \tag{A1}$$

$$V(r) = \frac{e^2}{\epsilon r}\mathrm{erf}\left(\frac{r}{2a}\right), \tag{A2}$$

$$z_{\sigma\tau} = \tau\frac{d_1 - \sigma d_2}{2} + D, \tag{A3}$$

where $\mathrm{erf}(x)$ is the error function and $D$ is the $z$-axis distance between the CQW centers. The intra-CQW potentials $u_{kk}(r)$, $k = 1$, or 2, are given by the same equation with $D = 0$ and the electron-hole separations $d_1$ and $d_2$ replaced by $d_k$. The plots of these potentials for parameter values representative of our experimental device are shown in Fig. 6. At $r \ll a$ all of them approach constant finite values, and at large $r$, these potentials behave as $1/r^3$. Potentials $u_{11}(r)$ and $u_{22}(r)$ are strictly repulsive. The potential $u_{12}(r)$ is attractive in the range of distances $r$ selected for the plot. At larger $r$, it eventually becomes repulsive, but it is already very small at such $r$.

The potentials $u_{ij}(r)$ serve as inputs to our computer program that computes many-body properties within the zero-temperature HNC formalism. Another input parameter is the effective-mass $m_{IX}$ of the excitons, which we took to be 0.2 of the free-electron mass $m_0$. Our implementation of the HNC

method is based on Ref. [54]. The output of these calculations include the pair-correlation functions $G_{ij}(r)$, the energy density $\varepsilon = \varepsilon(n_1, n_2)$, and the chemical potentials,

$$\mu_j = \partial\varepsilon/\partial n_j, \tag{A4}$$

of the excitons as functions of their number densities $n_1$ and $n_2$ in the CQWs. If the shake-up effects, i.e., many-body relaxation processes following the exciton recombination, can be neglected, then the exciton emission energies (or exciton "single-particle energies") $E_j$ should coincide with their chemical potentials,

$$E_j \approx \mu_j. \tag{A5}$$

Based on this assumption, we have constructed the plot of $\Delta E_1$ vs $\Delta E_2$ shown in Fig. 4(g) of the main text. Representative intra-CQW and inter-CQW pair-correlation functions are plotted in Figs. 4(b) and 4(e). At short distances, these functions show a deep "correlation hole" for excitons of the same CQW and a strong correlation peak for excitons of different CQWs.

### 2. Biexciton binding energy

From previous theoretical work on double-layer bosonic systems with repulsive intralayer and attractive interlayer dipolar interactions [43–46], we expect that the exciton system at low enough equal densities $n_1 = n_2$ should be made of bound pairs, the inter-CQW biexcitons. If $n_1 \neq n_2$, then biexcitons and unpaired excitons may coexist. A rough estimate of the required density is given by the Mott criterion stating that the biexcitons should appear when the dimensionless parameter $\min(n_1, n_2)b^2$ is less than some critical number, which is usually numerically small, perhaps, 0.02. Here $b$
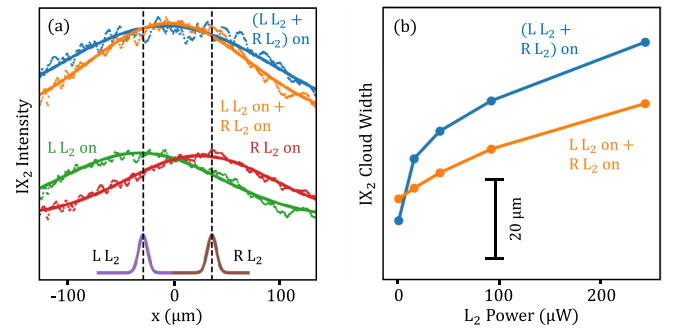


FIG. 8. Repulsion between the IX$_2$ clouds: Experiment. (a) The IX$_2$ cloud profiles when only the left L$_2$ is on (L L$_2$ on, green line), when only the right L$_2$ is on (R L$_2$ on, red line), and when both left and right L$_2$'s are on [(L L$_2$ + R L$_2$) on, blue line]. The sum of L L$_2$ on profile and R L$_2$ on profile (L L$_2$ on + R L$_2$ on) is shown by the orange line. Profile (L L$_2$ + R, L$_2$) on is wider than the sum of L, L$_2$ on profile and R, L$_2$ on profile, indicating the repulsion between the IX$_2$ clouds. The profiles of the left and right L$_2$ laser excitation spots are shown by purple and brown lines, respectively. The dashed lines indicate the centers of the excitation spots. (b) The width of the IX$_2$ cloud when both left and right L$_2$'s are on [(L L$_2$ + R L$_2$) on, blue points] in comparison to the width of the IX$_2$ cloud obtained as the sum of L L$_2$ on the cloud and R L$_2$ on the cloud [L L$_2$ on + R L$_2$ on, orange points] as a function of $P_{L2}$.
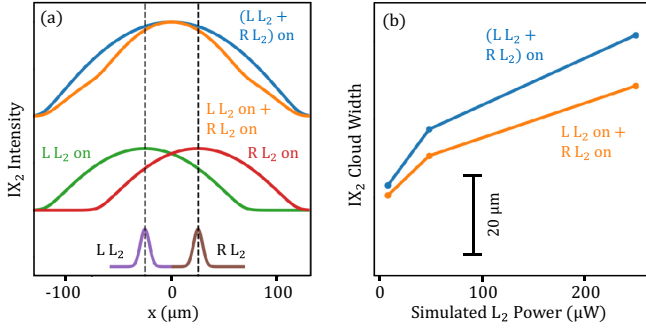
FIG. 9. Repulsion between the $IX_2$ clouds: Theory. (a) The $IX_2$ cloud profiles simulated when only the left $L_2$ is on (L $L_2$ on, green line), when only the right $L_2$ is on (R $L_2$ on, red line), and when both left and right $L_2$'s are on [(L $L_2$ + R $L_2$) on, blue line]. The sum of simulated L $L_2$ on profile and R $L_2$ on profile (L $L_2$ on + R $L_2$ on) is shown by the orange line. The profile (L $L_2$ + R $L_2$) on is wider than the sum of L $L_2$ on the profile and R $L_2$ on the profile, indicating the repulsion between the $IX_2$ clouds. The profiles of the left and right $L_2$ laser excitation spots are shown by purple and brown lines, respectively. The dashed lines indicate the centers of the excitation spots. (b) The width of the simulated $IX_2$ cloud when both left and right $L_2$'s are on [(L $L_2$ + R $L_2$) on, blue points] in comparison to the width of the $IX_2$ cloud obtained as the sum of simulated L $L_2$ on the cloud and R $L_2$ on the cloud [L $L_2$ on + R $L_2$ on, orange points] as a function of $P_{L2}$.

is the spatial size of the biexciton. Within our rigid-body approximation, the biexciton bound state can be easily found numerically. In the relative coordinates, this problem reduces to solving a Schrödinger equation for a particle of reduced mass $m_{IX}/2$ subject to the confining potential $u_{12}(r)$. For the same parameters as in Fig. 6, we obtained the binding energy to be $E_b = 0.286$ meV. From Fig. 7 we deduce the spatial size of the biexciton to be $b \sim 30$ nm so that the Mott critical density for biexcitons is on the order of $10^{10}$ cm$^{-2}$, not too far from the exciton densities realized in our experiment.

The following argument suggests that $E_b$ is, in fact, the maximum possible shift of the single-particle energies due to the inter-CQW attraction. Indeed, in the limit of high densities where average intra-CQW exciton separation is smaller

than $D$, correlations are negligible. At intermediate densities where HNC should be accurate, the dependence of, say, $E_1 = E_1(n_1, n_2)$ on $n_2$ with $n_1$ held fixed is either monotonic or flat within computational accuracy, see Figs. 4(c) and 4(f). Therefore, the asymptotic limit $n_1 = n_2 \rightarrow 0$ where all excitons are paired and

$$E_1 = E_2 = -E_b \qquad (A6)$$

should correspond to the largest possible attraction effect. Note that the HNC method reproduces this asymptotic limit only approximately. The tendency toward pairing is manifested in the aforementioned peak in the pair-correlation function $G_{12}(r)$ at $r = 0$. The shape of this peak computed by the HNC resembles the probability distribution of the biexciton, cf. Figs. 4(b) and 7. The integrated weight $N = n_2 \int G_{12}(r) d^2 r$ of the peak (where the integration extends up to $r \sim b$) is the average number of excitons of $CQW_1$ attracted to an exciton in $CQW_2$. When the biexcitons form, $N$ should approach unity. Yet within our HNC calculations $N$ keeps increasing as $n_1 = n_2$ decreases. This suggests that the standard HNC method is inadequate in the low-density regime where we should instead use Eq. (A6).

We found both in experimental measurements [Fig. 2(a) and 2(c)] and theoretical simulations [Figs. 4(a) and 4(c)] that increasing density of IXs in one layer causes a monotonic energy reduction for IXs in the other layer. These results differ with the results of Refs. [49,50] where a nonmonotonic dependence on the density was reported. The nonmonotonic dependence on the density was attributed to many-body polaron effects in Refs. [49,50]. Our simulations show no indication for the nonmonotonic dependence on the density.

The experiment still poses a challenge for the theory because the shift of $E_1$ has been observed to routinely exceed the computed $E_b = 0.286$ meV, see Fig. 2(a). To identify a possible reason for the discrepancy, we examined this important parameter more critically. First, we tested the validity of the rigid-body approximation. We used a previously developed computational tool [34] to accurately solve for the exciton and biexciton binding energies as two-body and four-body problems, respectively. For the parameters of Fig. 6 we obtained $E_b = 0.33$ meV. Hence, the rigid-body approximation is not the major source of the discrepancy. Next, we noted that $E_b$ is
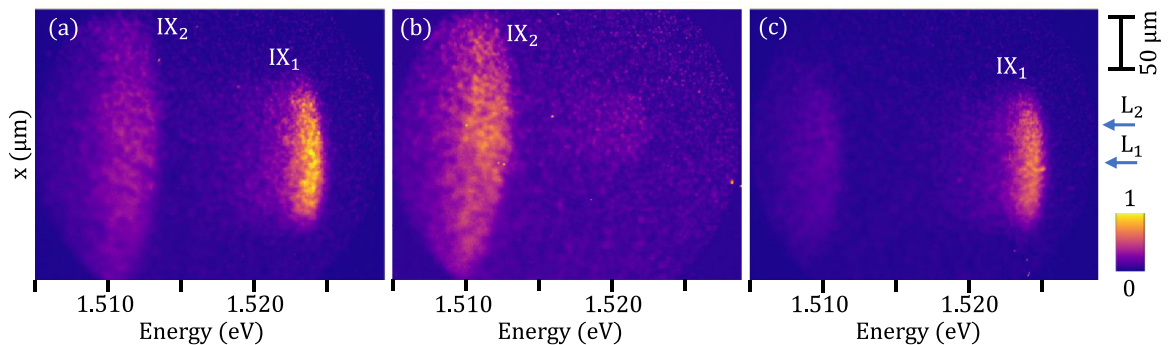


FIG. 10. Position-energy images of IX luminescence. (a) Both $L_2$ and $L_1$ lasers are on. (b) Only $L_2$ is on. (c) Only $L_1$ is on. The arrows indicate the excitation spot positions of the $L_2$ and $L_1$ lasers resonant to direct excitons in 15-nm CQW and 12-nm CQW, respectively. $L_2$ generates $IX_2$. $L_1$ generates $IX_1$ and a smaller concentration of $IX_2$. The laser powers $P_{L1} = 10 \mu W$, $P_{L2} = 250 \mu W$. Gate voltage $V_g = -2.0$ V and temperature $T = 1.7$ K.

greatly reduced compared to the depth $\approx 2$ meV of the potential well $u_{12}(r)$. This reduction is due to the zero-point motion. As an illustration of how this quantum effect may affect the binding energy, we recalculated $E_b$ and the wave functions of biexcitons for reduced masses enhanced two- and 20-fold. In the latter case, the binding energy rises to 1.16 meV, see Fig. 7, which is close to the experimentally measured shifts of $E_1$ we attributed to the inter-CQW attraction. It is hard to expect that the exciton mass is indeed enhanced by such an enormous factor due to the interaction alone. (As a point of reference, only a relatively weak interaction-induced mass enhancement, up to 25%, was observed in electron-hole systems in single QWs [57].) However, the suppression of the zero-point motion of an exciton pair may, in principle, be facilitated by disorder in the system that traps the excitons close together in deep potential wells.

## APPENDIX B: DYNAMICS OF EXCITON DENSITY DISTRIBUTION

In this Appendix we summarize the set of equations we used to model the macroscopic dynamics of excitons. To simplify the modeling, we assumed that the exciton densities $n_k$ and currents $j_k$ were functions of a single spatial coordinate $x$. These quantities obey the continuity equation,

$$\partial_t n_k(x,t) = \partial_x j_k + g_k(x,t) - n_k/\tau_k, \tag{B1}$$

where $\tau_k$ is the lifetime of the excitons in the $k$th CQW, which is known from the experiment, and $g_k$ is the generation rate proportional to the local laser power. To represent the exciton currents, we used the drift-diffusion approximation,

$$j_k(x,t) = -D_k \partial_x n_k(x,t) - B_k n_k(x,t)\partial_x \mu_k, \tag{B2}$$

where $D_k$ and $B_k = D_k/T$ are the diffusion coefficient and the drift mobility, respectively. Finally, to simplify the treatment of interaction effects, we linearized the density dependence of the exciton chemical potentials such that

$$\mu_1 = \gamma_{11} n_1 + \gamma_{12} n_2, \quad \mu_2 = \gamma_{22} n_2 + \gamma_{12} n_1, \tag{B3}$$

where $\gamma_{ij}$'s are interacting constants. Based on the simulations presented in Figs. 4(a) and 4(d) of the main text, we set the constants to be $\gamma_{11} = 9.3$, $\gamma_{22} = 11$, and $\gamma_{12} = -0.2$, all in units of $10^{-11}$ meV cm$^{-2}$. [Note that the intra-CQW coupling constants are 1/3 of the plate capacitor values, i.e., $\gamma_{kk} = (1/3)(4\pi e^2 d_k/\epsilon)$.] We developed a computer program that solves these coupled equations on a discrete grid of $x$ as a function of the time-variable $t$, starting from initial conditions $n_1 = n_2 \equiv 0$. To get a relation between the laser powers and the generation rates, we fitted the shifts $E_k \approx \mu_k$ of the exciton
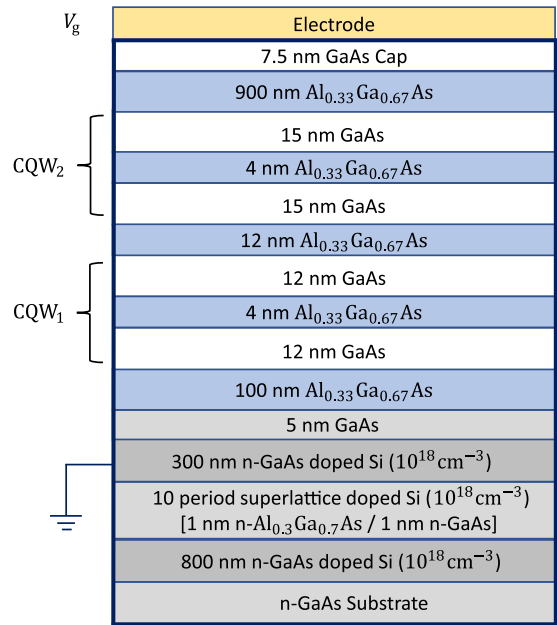


FIG. 11. Cross section of the two-CQW heterostructure. The thicknesses and doping concentrations of the layers are indicated.

emission energies measured as functions of the laser power to the results of these simulations. We estimated the diffusion coefficients $D_k$ by fitting the calculated width of the IX$_1$ and IX$_2$ exciton clouds to the measured widths of these clouds generated selectively by L$_1$ or L$_2$.

As outlined in the main text, the simulations show that the IX$_1$ cloud attracts to the IX$_2$ cloud (Fig. 5), in qualitative agreement with the attraction observed in the experiment (Fig. 3). In comparison, both our experimental measurements (Fig. 8) and our theoretical simulations (Fig. 9) show that the two clouds of repulsively interacting IX$_2$ repel each other.

## APPENDIX C: POSITION-ENERGY LUMINESCENCE IMAGES

The differential $x$-energy image [Fig. 1(b)] is obtained by subtracting the $x$-energy images created by only L$_1$ on [Fig. 10(c)] and by only L$_2$ on [Fig. 10(b)] from the $x$-energy image created by both lasers on simultaneously [Fig. 10(a)].

## APPENDIX D: CROSS SECTION OF THE HETEROSTRUCTURE

The cross section of the two-CQW heterostructure showing the thicknesses and doping concentrations of the layers is presented in Fig. 11.

[1] Y. E. Lozovik and V. I. Yudson, A new mechanism for superconductivity: pairing between spatially separated electrons and holes, Zh. Eksp. Teor. Fiz. **71**, 738 (1976) [Sov. Phys. JETP **44**, 389 (1976)].

[2] D. Yoshioka and A. H. Macdonald, Double quantum well electron-hole systems in strong magnetic fields, J. Phys. Soc. Jpn. **59**, 4211 (1990).

[3] L. V. Butov, A. Zrenner, G. Abstreiter, G. Böhm, and G. Weimann, Condensation of Indirect Excitons in Coupled AlAs/GaAs Quantum Wells, Phys. Rev. Lett. **73**, 304 (1994).

[4] X. Zhu, P. B. Littlewood, M. S. Hybertsen, and T. M. Rice, Exciton Condensate in Semiconductor Quantum Well Structures, Phys. Rev. Lett. **74**, 1633 (1995).

[5] Y. E. Lozovik and O. L. Berman, Phase transitions in a system of spatially separated electrons and holes, J. Exp. Theor. Phys. **84**, 1027 (1997)].

[6] L. V. Butov, A. A. Shashkin, V. T. Dolgopolov, K. L. Campman, and A. C. Gossard, Magneto-optics of the spatially separated electron and hole layers in GaAs/Al$_x$Ga$_{1-x}$As coupled quantum wells, Phys. Rev. B **60**, 8753 (1999).

[7] L. V. Butov, A. C. Gossard, and D. S. Chemla, Macroscopically ordered state in an exciton system, Nature (London) **418**, 751 (2002).

[8] A. L. Ivanov, Quantum diffusion of dipole-oriented indirect excitons in coupled quantum wells, Europhys. Lett. **59**, 586 (2002).

[9] A. L. Ivanov, L. E. Smallwood, A. T. Hammack, S. Yang, L. V. Butov, and A. C. Gossard, Origin of the inner ring in photoluminescence patterns of quantum well excitons, Europhys. Lett. **73**, 920 (2006).

[10] M. Remeika, J. C. Graves, A. T. Hammack, A. D. Meyertholen, M. M. Fogler, L. V. Butov, M. Hanson, and A. C. Gossard, Localization-Delocalization Transition of Indirect Excitons in Lateral Electrostatic Lattices, Phys. Rev. Lett. **102**, 186803 (2009).

[11] M. Hagn, A. Zrenner, G. Böhm, and G. Weimann, Electric-field-induced exciton transport in coupled quantum well structures, Appl. Phys. Lett. **67**, 232 (1995).

[12] Z. Vörös, R. Balili, D. W. Snoke, L. Pfeiffer, and K. West, Long-Distance Diffusion of Excitons in Double Quantum Well Structures, Phys. Rev. Lett. **94**, 226401 (2005).

[13] A. Gärtner, A. W. Holleitner, J. P. Kotthaus, and D. Schuh, Drift mobility of long-living excitons in coupled GaAs quantum wells, Appl. Phys. Lett. **89**, 052108 (2006).

[14] S. Lazić, P. V. Santos, and R. Hey, Exciton transport by moving strain dots in GaAs quantum wells, Physica E **42**, 2640 (2010).

[15] A. V. Gorbunov, V. B. Timofeev, and D. A. Demin, Electro-Optical Trap for Dipolar Excitons in a GaAs/AlAs Schottky Diode with a Single Quantum Well, JETP Lett. **94**, 800 (2011).

[16] M. Alloing, A. Lemaître, E. Galopin, and F. Dubin, Nonlinear dynamics and inner-ring photoluminescence pattern of indirect excitons, Phys. Rev. B **85**, 245106 (2012).

[17] S. Lazić, A. Violante, K. Cohen, R. Hey, R. Rapaport, and P. V. Santos, Scalable interconnections for remote indirect exciton systems based on acoustic transport, Phys. Rev. B **89**, 085313 (2014).

[18] C. J. Dorow, M. W. Hasling, D. J. Choksy, J. R. Leonard, L. V. Butov, K. W. West, and L. N. Pfeiffer, High-mobility indirect excitons in wide single quantum well, Appl. Phys. Lett. **113**, 212102 (2018).

[19] S. Ben-Tabou de Leon and B. Laikhtman, Mott transition, biexciton crossover, and spin ordering in the exciton gas in quantum wells, Phys. Rev. B **67**, 235315 (2003).

[20] R. Zimmermann and C. Schindler, Exciton-exciton interaction in coupled quantum wells, Solid State Commun. **144**, 395 (2007).

[21] C. Schindler and R. Zimmermann, Analysis of the exciton-exciton interaction in semiconductor quantum wells, Phys. Rev. B **78**, 045313 (2008).

[22] Y. E. Lozovik, I. L. Kurbakov, G. E. Astrakharchik, J. Boronat, and M. Willander, Strong correlation effects in 2D Bose-Einstein condensed dipolar excitons, Solid State Commun. **144**, 399 (2007).

[23] B. Laikhtman and R. Rapaport, Exciton correlations in coupled quantum wells and their luminescence blue shift, Phys. Rev. B **80**, 195313 (2009).

[24] A. L. Ivanov, E. A. Muljarov, L. Mouchliadis, and R. Zimmermann, Comment on "Photoluminescence Ring Formation in Coupled Quantum Wells: Excitonic Versus Ambipolar Diffusion", Phys. Rev. Lett. **104**, 179701 (2010).

[25] K. Cohen, R. Rapaport, and P. V. Santos, Remote Dipolar Interactions for Objective Density Calibration and Flow Control of Excitonic Fluids, Phys. Rev. Lett. **106**, 126402 (2011).

[26] M. Remeika, J. R. Leonard, C. J. Dorow, M. M. Fogler, L. V. Butov, M. Hanson, and A. C. Gossard, Measurement of exciton correlations using electrostatic lattices, Phys. Rev. B **92**, 115311 (2015).

[27] Yu. E. Lozovik and O. L. Berman, Phase transitions in a system of two coupled quantum wells, JETP Lett. **64**, 573 (1996).

[28] S. De Palo, F. Rapisarda, and G. Senatore, Excitonic Condensation in a Symmetric Electron-Hole Bilayer, Phys. Rev. Lett. **88**, 206401 (2002).

[29] G. E. Astrakharchik, J. Boronat, I. L. Kurbakov, and Y. E. Lozovik, Quantum Phase Transition in a Two-Dimensional System of Dipoles, Phys. Rev. Lett. **98**, 060405 (2007).

[30] J. Schleede, A. Filinov, M. Bonitz, and H. Fehske, Phase Diagram of Bilayer Electron-Hole Plasmas, Contrib. Plasma Phys. **52**, 819 (2012).

[31] R. A. Suris, Gas-Crystal Phase Transition in a 2D Dipolar Exciton System, J. Exp. Theor. Phys. **122**, 602 (2016).

[32] For structures with small $d$, the intralayer dipolar IX repulsion weakens that can stabilize intralayer biexcitons [21,33–35].

[33] M. Y. J. Tan, N. D. Drummond, and R. J. Needs, Exciton and biexciton energies in bilayer systems, Phys. Rev. B **71**, 033303 (2005).

[34] A. D. Meyertholen and M. M. Fogler, Biexcitons in two-dimensional systems with spatially separated electrons and holes, Phys. Rev. B **78**, 235307 (2008).

[35] R. Maezono, P. López Ríos, T. Ogawa, and R. J. Needs, Excitons and Biexcitons in Symmetric Electron-Hole Bilayers, Phys. Rev. Lett. **110**, 216407 (2013).

[36] H. Kadau, M. Schmitt, M. Wenzel, C. Wink, T. Maier, I. Ferrier-Barbut, and T. Pfau, Observing the Rosensweig instability of a quantum ferrofluid, Nature (London) **530**, 194 (2016).

[37] I. Ferrier-Barbut, H. Kadau, M. Schmitt, M. Wenzel, and T. Pfau, Observation of Quantum Droplets in a Strongly Dipolar Bose Gas, Phys. Rev. Lett. **116**, 215301 (2016).

[38] L. Tanzi, E. Lucioni, F. Famà, J. Catani, A. Fioretti, C. Gabbanini, R. N. Bisset, L. Santos, and G. Modugno, Observation of a Dipolar Quantum Gas with Metastable Supersolid Properties, Phys. Rev. Lett. **122**, 130405 (2019).

[39] F. Böttcher, J.-N. Schmidt, M. Wenzel, J. Hertkorn, M. Guo, T. Langen, and T. Pfau, Transient Supersolid Properties in an Array of Dipolar Quantum Droplets, Phys. Rev. X **9**, 011051 (2019).

[40] L. Chomaz, D. Petter, P. Ilzhöfer, G. Natale, A. Trautmann, C. Politi, G. Durastante, R. M. W. van Bijnen, A. Patscheider, M. Sohmen, M. J. Mark, and F. Ferlaino, Long-Lived and Transient Supersolid Behaviors in Dipolar Quantum Gases, Phys. Rev. X **9**, 021012 (2019).

[41] B. Wunsch, N. T. Zinner, I. B. Mekhov, S.-J. Huang, D.-W. Wang, and E. Demler, Few-Body Bound States in Dipolar

Gases and Their Detection, Phys. Rev. Lett. **107**, 073201 (2011).

[42] M. Dalmonte, P. Zoller, and G. Pupillo, Trimer Liquids and Crystals of Polar Molecules in Coupled Wires, Phys. Rev. Lett. **107**, 163202 (2011).

[43] X. Lu, C.-Q. Wu, A. Micheli, and G. Pupillo, Structure and melting behavior of classical bilayer crystals of dipoles, Phys. Rev. B **78**, 024108 (2008).

[44] A. Safavi-Naini, Ş. G. Söyler, G. Pupillo, H. R. Sadeghpour, and B. Capogrosso-Sansone, Quantum phases of dipolar bosons in bilayer geometry, New J. Phys. **15**, 013036 (2013).

[45] A. Macia, G. E. Astrakharchik, F. Mazzanti, S. Giorgini, and J. Boronat, Single-particle versus pair superfluidity in a bilayer system of dipolar bosons, Phys. Rev. A **90**, 043623 (2014).

[46] F. Cinti, D.-W. Wang, and M. Boninsegni, Phases of dipolar bosons in a bilayer geometry, Phys. Rev. A **95**, 023622 (2017).

[47] The dipolar interaction $v(r) \propto 1/r^3$ is long range for three-dimensional and short range for two-dimensional and one-dimensional systems.

[48] K. Cohen, M. Khodas, B. Laikhtman, P. V. Santos, and R. Rapaport, Vertically coupled dipolar exciton molecules, Phys. Rev. B **93**, 235310 (2016).

[49] C. Hubert, Y. Baruchi, Y. Mazuz-Harpaz, K. Cohen, K. Biermann, M. Lemeshko, K. West, L. Pfeiffer, R. Rapaport, and P. Santos, Attractive Dipolar Coupling between Stacked Exciton Fluids, Phys. Rev. X **9**, 021026 (2019).

[50] C. Hubert, K. Cohen, A. Ghazaryan, M. Lemeshko, R. Rapaport, and P. V. Santos, Attractive interactions, molecular complexes, and polarons in coupled dipolar exciton fluids, Phys. Rev. B **102**, 045307 (2020).

[51] A. T. Hammack, N. A. Gippius, Sen Yang, G. O. Andreev, L. V. Butov, M. Hanson, and A. C. Gossard, Excitons in electrostatic traps, J. Appl. Phys. **99**, 066104 (2006).

[52] Y. Y. Kuznetsova, J. R. Leonard, L. V. Butov, J. Wilkes, E. A. Muljarov, K. L. Campman, and A. C. Gossard, Excitation energy dependence of the exciton inner ring, Phys. Rev. B **85**, 165452 (2012).

[53] Due to the longer $IX_2$ lifetime, the $IX_2$ PL signal is lower than the $IX_1$ PL signal, and the $IX_2$ cloud is wider than the $IX_1$ cloud. These factors make the accuracy of determining the $IX_2$ cloud shift too low to analyze this shift.

[54] T. Chakraborty, Structure of binary boson mixtures at $T = 0$ K, Phys. Rev. B **26**, 6131 (1982).

[55] S. H. Abedinpour, R. Asgari, and M. Polini, Theory of correlations in strongly interacting fluids of two-dimensional dipolar bosons, Phys. Rev. A **86**, 043601 (2012).

[56] L. V. Butov, C. W. Lai, D. S. Chemla, Y. E. Lozovik, K. L. Campman, and A. C. Gossard, Observation of Magnetically Induced Effective-Mass Enhancement of Quasi-2D Excitons, Phys. Rev. Lett. **87**, 216804 (2001).

[57] L. V. Butov, V. D. Egorov, V. D. Kulakovskii, and T. G. Anderson, Magnetoluminescence study of many-body effects in a dense electron-hole plasma of strained $In_xGa_{1-x}As$/GaAs quantum wells, Phys. Rev. B **46**, 15156 (1992).

[58] M. Sammon and B. I. Shklovskii, Attraction of indirect excitons in van der Waals heterostructures with three semiconducting layers, Phys. Rev. B **99**, 165403 (2019).

[59] E. V. Calman, L. H. Fowler-Gerace, D. J. Choksy, L. V. Butov, D. E. Nikonov, I. A. Young, S. Hu, A. Mishchenko, and A. K. Geim, Indirect Excitons and Trions in $MoSe_2$/$WSe_2$ van der Waals Heterostructures, Nano Lett. **20**, 1869 (2020).